Spatiotemporal Ocean Tidal Loading in InSAR Measurements Determined by Kinematic PPP Solutions of a Regional GPS Network

Wei Peng, Qijie Wang, F. Benjamin Zhan, and Yunmeng Cao

***Abstract*—The coastal crustal deformation caused by ocean tidal loading (OTL) varies spatially and temporally, and this spatiotemporal variation in satellite-based interferometric synthetic aperture radar (InSAR) measurements needs to be determined. In this article, we propose a spatiotemporal modeling method to estimate the OTL displacements in InSAR measurements using the kinematic precise point positioning (PPP) solutions of a regional GPS network. We tested the method through an experiment using 25 Sentinel-1B images and long-term observations of 172 GPS reference sites from Southern California. The experimental results suggest that there are significant OTL and solid Earth tide effects in the differential InSAR interferogram, which is greater than 40 mm. We find that the spatial characteristics of OTL variations can be expressed as a high-order polynomial in the two variables of latitude and longitude, and the spatiotemporally modeled PPP tidal estimates of the high-density GPS sites can provide high precision OTL correction for all the pixels in the interferogram. In the last part of the study, we show that the spatial large-scale signals in the differential interferograms of Sentinel-1B data are mainly atmospheric delay, solid Earth tidal, and OTL effect, and demonstrate the importance of the tidal correction in the InSAR measurements.**

***Index Terms*—InSAR measurements, kinematic PPP tidal displacements, least-squares support vector machine, ocean tidal loading.**

I. Introduction

The Interferometric synthetic aperture radar (InSAR) is a powerful tool for mapping the Earth's ground displacements, and the Sentinel-1 measurements in coastal areas usually contain tectonic deformation, atmospheric delay, the ocean tidal loading (OTL) effect, solid Earth tidal (SET) effect, orbital error, residual topographic phase error, and decorrelation noise [1]–[3]. The OTL effect is the response of the solid Earth to ocean mass redistribution due to the gravitational force changes, its gradient nonlinearly decreases from cm/100-km scale in the coastal area to mm/100-km scale in the area 200 km away from the coast [4]–[6]. For the other spatial large-scale signals, the spatial wavelength of the SET effect is more than one order larger than the OTL effect, and its spatial variation in the range of the Sentinel-1 SLC image tends to be a lower-order curve [7]. The atmospheric delay maps provided by the Generic Atmospheric Correction Online Service for InSAR (GACOS) and precise orbital files are commonly used to reduce atmospheric delay and the orbital error [8], [9]. However, the residual signals of the atmospheric delay and orbital error in the differential InSAR (DInSAR) interferogram may introduce the spatial large-scale error in the determination of the OTL displacements, so we used the ocean tide models and kinematic precise point positioning (PPP) tidal estimates of a regional GPS network to analyze the temporal and spatial variation of the OTL effect in the InSAR measurements.

Tide models such as TPXO8, EOT11A, DTU10, FES2014b, and so on, are established by assimilating satellite altimeter or geodetic tide station data into a hydrodynamic model [10]–[12]. The tide models provide the tidal heights of the ocean to the Love-numbers-derived mass loading Green's function for calculating the OTL displacements [13], [14], but the accuracy of the OTL displacements depends on the computational method, Earth model, and tide model. The tide models have high precision in the deep ocean, but the precision is lower in offshore areas [15]. Therefore, some researchers have suggested that GPS tidal estimates can be used instead of tide model predictions in regions where tide models are less accurate or inaccurate [16], or where constraints are provided on the selection of the tide model at coastal stations [17].

As the number of GPS reference sites worldwide is growing continuously [18], [19], studies of the spatial feature of the OTL effect have become possible. There are dense GPS reference stations in Southern California that provide a lot of long-term GPS observations for building a spatial tidal constituent model. These GPS data of the ground-based network can measure the spatiotemporal displacement of the OTL effect directly. The kinematic and static PPP techniques have been proved to be able to estimate the OTL displacements in the temporal analysis of the OTL effect [20], [21]. In addition,

Manuscript received March 28, 2020; revised May 20, 2020; accepted May 31, 2020. Date of publication June 16, 2020; date of current version July 8, 2020. This work was supported in part by the National Natural Science Foundation of China under Grant U1531128 and Grant 41820104005, and in part by the Hunan Provincial Innovation Foundation for Postgraduate under Grant CX2017B053. The work of Wei Peng was supported by the China Scholarship Council for a 1-year study abroad. *(Corresponding author: Qijie Wang.)*

Wei Peng and Qijie Wang are with the School of Geosciences and Info-Physics, Central South University, Changsha 410083, China (e-mail: pengweicsu@csu.edu.cn; qjwang@csu.edu.cn).

F. Benjamin Zhan is with the Texas Center for Geographic Information Science Department of Geography, Texas State University, San Marcos, TX 78666 USA (e-mail: zhan@txstate.edu).

Yunmeng Cao is with the Division of Physical Sciences and Engineering, King Abdullah University of Science and Technology, Jeddah 23955, Kingdom of Saudi Arabia (e-mail: ymcmrs@gmail.com).

Digital Object Identifier 10.1109/JSTARS.2020.3002777

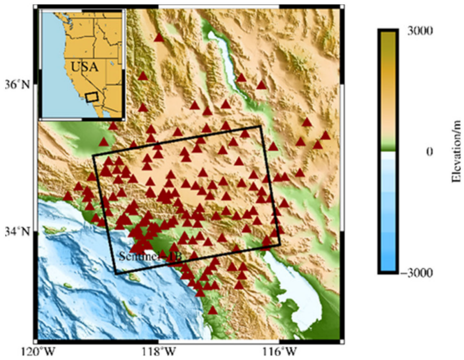

Fig. 1. Frame of the Sentinel-1B SAR image and distribution of the selected GPS sites in Southern California.

the parameters of the amplitude and phase delay of the tidal constituents in the temporal analysis relate to the spatial position, so that the *phasors* constructed by the amplitude and phase delay can reflect the spatial features of the tidal constituents [22].

We use the least-squares support vector machine (LSSVM) method to model the *phasors*, to avoid the problems of a small sample size, nonlinearity, high dimensions, and local minimization when predicting OTL correction of the pixels of the interferograms. The method transforms the low-dimensional nonlinear problem into a high-dimensional space by using kernel functions, and then obtains the optimal solution by solving the linear Karush–Kuhn–Tucker (KKT) system [23], [24]. We use the regression function of the LSSVM method when modeling the *phasors* of the tidal constituents. The kernel function of the LSSVM method is based on the spatial characteristics of the tidal constituents. The spatial trend of the OTL displacements from coast to inland is close to the bivariate polynomial [6]. In this article, we further consider the selection of the kernel function based on the spatial variation of the *phasors* of the tide model and the PPP tidal estimates.

II. Data Processing

An area covering Southern California and its adjoining ocean was selected as the study site for analyzing the OTL effect in the InSAR measurements. The Sentinel-1B SLC image has high coherence in this area, and the distances between the GPS sites are 5–25 km in the SAR range. The frame of the Sentinel-1B SAR imageries and distribution of the 172 GPS reference sites are shown in Fig. 1.

A. InSAR Data Preprocessing

A total of 25 Sentinel-1B SLC images acquired between January 01, 2017 and December 01, 2017, were used in the experiment. The imaging time is about 01:49:00 UTC, and the revisit period is 12 days. The perpendicular baseline is less than 120 m (Fig. 2).

The procedures of image coregistration, interferogram generation, flat-earth phase removal, phase unwrapping, and geocoding were performed using GAMMA software [25]. The orbit file of the precise orbit ephemerides (POE) was added into the data processing. The topography phase was removed using the shuttle radar topography mission-1 (SRTM-1) digital elevation model (DEM), and the minimum cost flow (MCF) method was used for the phase unwrapping. The small baseline subset (SBAS) method was used for generating the time series of SAR measurements [26].

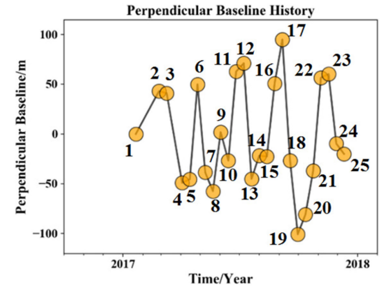

Fig. 2. Perpendicular baseline history of the SAR images.

TABLE I
INPUT FILES FOR THE KINEMATIC PPP PROCESSING

Name	Parameters or input files
Solid Earth tide	TIDE2000.TPO
Satellite clock	COD*****.clk
Precise ephemeris	COD*****.eph
Earth rotation parameters	COD*****.erp
Ionosphere maps	COD*****.ION
Differential code biases (DCBs)	P1C1****.DCB, P1P2****.DCB
Atmospheric tide correction and pole tide correction	Atmospheric tidal and pole tide model (IERS2010)
Ocean tide correction	No

B. GPS Data Preprocessing

GPS observations from January 01, 2014, to December 31, 2018 are available from the Scripps Orbit and Permanent Array Center (SOPAC). The GPS observations were processed by the standard procedures of Bernese GNSS software version 5.2[1] in kinematic PPP mode into ambiguity-float solutions [27]. The sample interval is 10 min; the elevation cutoff angle is 3°. The International GNSS Service (IGS) precise ephemeris, clock, and Earth rotation parameters were used, and the tropospheric mapping function used the gridded Vienna Mapping Function (VMF1). The Solid Earth tide, atmospheric tide and pole tide correction were included in the data processing, while the ocean tide loading correction was not (Table I).

The kinematic PPP coordinates time series were preprocessed to eliminate the outliers. The missing data are less than 30% of the PPP coordinate time series of the 172 GPS sites [16], as shown in Fig. 3.

Then, the noises of the PPP coordinate time series were reduced using a wavelet filter. The filtered PPP coordinates were converted to the north, east, and up directions, and then projected into the line-of-sight (LOS) direction of the SAR system [28].

[1]Online. [Available]: http://www.bernese.unibe.ch/docs/DOCU52.pdf

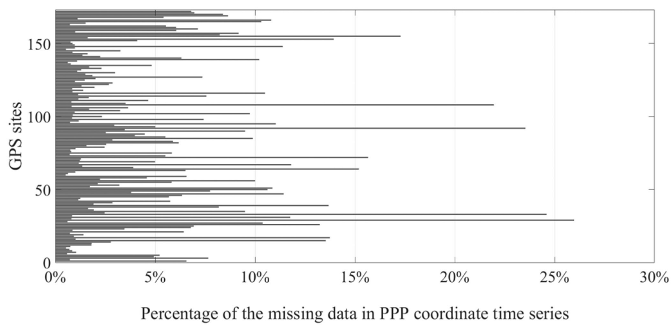

Fig. 3. Percentage of the missing data of the PPP coordinate time series of the 172 GPS sites.

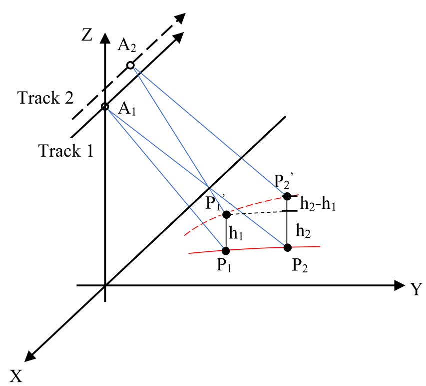

Fig. 4. Principle diagram of the InSAR and GPS measuring tides effect.

The incidence angles of the selected Sentinel-1B measurements are in the range of 27.34° to 39.80°, and the angle between the flight direction and the north direction of the satellite is $-12.98°$.

III. Methodology

InSAR deformation monitoring uses the differential phases to measure the changes of the crustal deformation. The spatial difference of the tides displacements between the GPS sites near sea P_1 and inland P_2 can be measured in the interferometric phase (Fig. 4).

The vector tides displacement of the $h_1$and h_2 can go up to several decimeters, and the largest spatial difference $h_2 - h_1$ in the LOS direction of the Sentinel-1B measurements is greater than 40 mm in this research. Therefore, the displacements of a pixel i in an unwrapped differential interferogram can be expressed as

$$d_i = d_i^{\mathrm{Tectonic}} + d_i^{\mathrm{OTL}} + d_i^{\mathrm{SET}} + d_i^{\mathrm{Atm}} + d_i^{\mathrm{Topo}} + \varepsilon_i \quad (1)$$

where d_i^{Tectonic} represents the tectonic crustal deformation; d_i^{OTL} is the OTL displacement; d_i^{SET} is the SET displacement; d_i^{Atm} is the atmospheric delay error; d_i^{Topo} represents the residual topographic phase; and ε_i is related to the phase unwrapping error, the decorrelation noise, etc.

According to the tide algorithm of the IERS convention 2010, the site SET displacement can be accurately estimated by the use of a two-step procedure [29]. While, the inaccuracy of the OTL displacements based on IERS 2010 mostly related to the tide models [16]. Therefore, the kinematic PPP coordinates in the LOS direction are modeled using a tidal harmonic function to improve the OTL displacements. The OTL displacement of eight diurnal and semidiurnal constituents can be written as [18]

TABLE II
Periods of the Main Tidal Constituents and Parameter $\omega_k t_p$

Constituent Symbol	Constituent Period/h	$\omega_k t_p$ /°
M2	12.421	67.15
S2	12.000	0
N2	12.658	-89.13
K2	11.967	23.83
K1	23.935	11.73
O1	25.819	55.65
Q1	26.868	-101.13
P1	24.066	-11.85

$$d_n^{\mathrm{OTL}}(t) = \sum_{k=1}^{8} f_k A_{k,n} \cos(\omega_k t + \chi_k + \mu_k - \Phi_{k,n}) \quad (2)$$

where n is the nth GPS site, the spatial distribution density of GPS network depends on the spatial characteristics of the OTL deformation signal, preferably at less than 25-km level near the coast; A_k and $\Phi_k$are the amplitude and phase delay of a tidal constituent k, respectively; χ_k is the initial astronomical angle; ω_k is the angular frequency; f_k and μ_k are the node factor and the astronomical angle, respectively.

A. Temporal Analysis

The temporal features of the tidal constituents are related to the parameter $\omega_k t$. The displacements of the tidal constituents in (2) can be expressed as

$$d_{k,n}(t_p) = \left[\, f_k A_{k,n} \cos(B) \;\; -f_k A_{k,n} \sin(B) \,\right] \begin{bmatrix} \cos(\omega_k t_p) \\ \sin(\omega_k t_p) \end{bmatrix} \quad (3)$$

$$B = \chi_k + \mu_k - \Phi_{k,n} \quad (4)$$

where the $f_k A_{k,n} \cos(B)$ and $-f_k A_{k,n} \sin(B)$ are not related to the time change; t_p is the SAR imaging time. The characteristics of the time-varying parameter $\omega_k t_p$ depend on the revisit period of the SAR satellite and the period of the tidal constituents (Table II).

The revisit period of the SAR satellite is an integral multiple of the period of constituent S2, so the effect of constituent S2 on the SAR measurements is an offset. The time varying of the vector composed of the $\cos(\omega_k t_p)$ and $\sin(\omega_k t_p)$ in (3) for the first 10 Sentinel-1B SAR images are shown in Fig. 5.

B. Spatial Analysis

The parameters of the amplitude and phase lag are related to the locations of the GPS sites. The tidal constituent $k$in (2) can also be transferred to

$$d_{k,n}(t) = \left[\, f_k \cos(\omega_k t + \chi_k + \mu_k) \;\; f_k \sin(\omega_k t + \chi_k + \mu_k) \,\right]$$

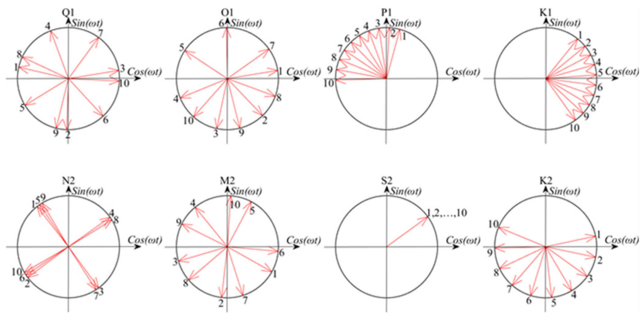

Fig. 5. Time-varying characteristics of the tidal constituents at 12-day intervals for the first 10 Sentinel-1B SAR images

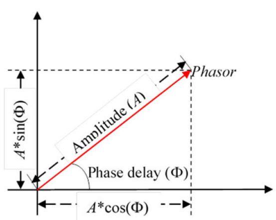

Fig. 6. *Phasor* constructed by the amplitude A and phase delay Φ of a tidal constituent.

$$\times \begin{bmatrix} A_{k,n}\cos(\Phi_{k,n}) \\ A_{k,n}\sin(\Phi_{k,n}) \end{bmatrix}. \tag{5}$$

The spatial characteristics of the tidal constituents are determined by the $\mathrm{Phasor}_{k,n}$ constructed by the amplitude $A_{k,n}$ and phase delay $\Phi_{k,n}$

$$\mathrm{Phasor}_{k,n} = (A_{k,n}\cos(\Phi_{k,n}), A_{k,n}\sin(\Phi_{k,n}))_i. \tag{6}$$

The vector construction of the *phasor* of a tidal constituent in the (6) is shown in Fig. 6.

To predict $\mathrm{Phasor}_{k,i}$ at the pixel i of the interferogram, the $\mathrm{Phasor}_{k,n}$ of the$N$ GPS sites are modeled using the LSSVM method. The Phasor_n of a tidal constituent and the spatial positions of the GPS sites are taken as training samples $S = (x_n, y_n),\quad n = 1, \ldots, N$, where $x_n \in R^2$ denotes the longitude and latitude of the $n$thGPS site, and $y_n \in R$ denotes the $\mathrm{Phasor}_{k,n}$ of the tidal constituent. The theoretical regression model of the LSSVM method is expressed as follows:

$$y = w^T \bullet \varphi(x) + \beta \tag{7}$$

where w is the weight coefficient vector, $\varphi(\bullet)$ is the mapping function that maps the samples into the high-dimensional feature space, and β is a bias term.

Based on the principle of structural risk minimization and the KKT optimum condition, the (7) can be transferred to a least-squares regression model

$$y = \sum_{n=1}^{N} \alpha_n H(x, x_n) + \beta \tag{8}$$

where $\alpha_n (n = 1, \ldots, N)$ is the Lagrange multiplier, and $H(x, x_n)$ is the kernel function.

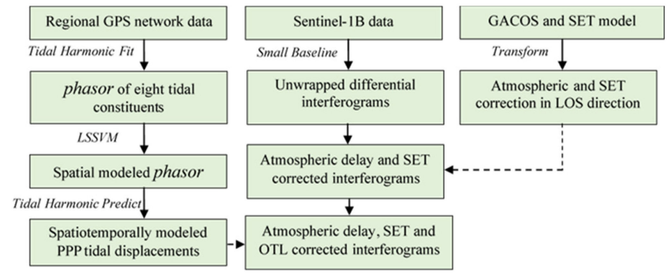

Fig. 7. Flowchart of spatiotemporal analysis of the OTL effect in the Sentinel-1B data

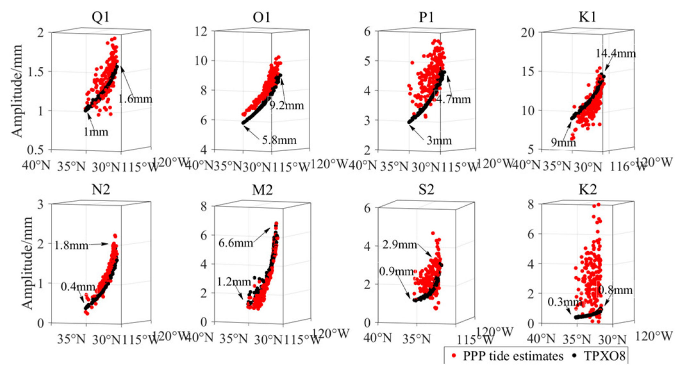

Fig. 8. Comparison of the amplitudes of the tidal constituents between the TPXO8 tide model and the PPP tidal estimates.

C. Flowchart of Spatiotemporal OTL Analysis

The flowchart of the spatiotemporal analysis of the OTL effect in the Sentinel-1B data is shown in Fig. 7.

IV. Spatial and Temporal Analysis of the Tidal Constituents in InSAR Measurements

The variation of the tidal constituents is vector variation in high-dimensional space, which is related to the horizontal position, the *phasors* of the tidal constituents, the periods of the tidal constituents, and the SAR satellite revisit.

A. Spatial Analysis of the Tidal Constituents

The parameters of the amplitude and phase delay of the tidal constituents in the GPS sites were estimated using (2). Meanwhile, the tidal parameters of the TPXO8 tide model were also calculated using the Some Programs for Ocean-Tide Loading (SPOTL) software [30]. We compare the amplitudes of the tidal constituents between the TPXO8 tide model and the PPP tidal estimates, which is shown in Fig. 8.

We analyzed the eight tidal constituents in magnitude, precision, and spatial features based on the results shown in Fig. 8. According to the TPXO8 tide model, the maximum spatial difference of the amplitudes of the M2 constituent is 5.4 mm, and that of the K1 and O1 constituents is 5.3 and 3.4 mm, respectively. The smallest spatial difference is constituent K2 (less than 0.5 mm). The amplitudes of the M2, O1, and N2 constituents calculated using PPP tidal estimates have higher precision, and the constituent K2 has the largest error with the smallest spatial difference. In previous studies, the bias of the constituents K1 and K2 was found to be related to GPS satellite orbit errors and the multipath effect of the GPS station [31]–[33]. Therefore, we used the *phasor* of the constituent K2 of the tide model to replace the *phasor* estimated by the PPP tidal method.

The *phasor* of the Q1, O1, P1, K1, N2, and M2 constituents were estimated using the kinematic PPP solutions. Meanwhile, the *phasors* of the tidal constituents of the TPXO8 tide model were calculated. We compare the *phasor* of the PPP tidal estimates and TPXO8 tide model, and the vector differences of the *phasor* (Fig. 9).

The vector length and direction of the *phasor* differences between PPP tidal estimates and TPXO8 tide model are similar, and the difference of the amplitude and phase delay are shown in Fig. 10.

In the Fig. 10, the differences of the amplitude and phase delay of the tide constituents are considered as systematic bias. The systematic bias of PPP tidal estimates generally involves the solid Earth tide model uncertainties, atmospheric tide loading, tidal geocentric motions, GPS orbit errors, and higher-order ionosphere effects, and the tide models have lower precision in offshore areas [34].

The spatial features of the tidal constituents of the GPS network are close to a high-order polynomial in the two variables of latitude and longitude, and the orders of the polynomial functions for the eight tidal constituents are different. The polynomial kernel of the LSSVM method in (8) can be written as

$$H(x, x_n) = \left(x^T x_n + e\right)^r \tag{9}$$

where e is the intercept and r is the degree of the polynomial. The optimal degrees of the tide constituents of the PPP tide estimates are 3,4,4,3,4, and 4, and the optimal degrees of the Q1, O1, P1, K1, N2, and M2 constituents based on TPXO8 model are 3,3,3,3,4, and 4. Based on the determined polynomial kernel, the *phasors* of the tidal constituents of the GPS sites are modeled using LSSVM method. The Lagrange multiplier and bias terms in the (8) are calculated to predict the *phasors* of the pixels in the differential interferogram.

The PPP tidal estimates in SAR images can be calculated according to sptial modeled *phasor*. To evaluate the spatiotemporally modeled PPP tidal estimates, the RMSE values of the differences between the spatiotemporally modeled PPP tidal estimates and the tide models (DTU10, EOT11A, TPXO8, FES2014b, and HAMTIDE) in the 25 SAR images were calculated (Fig. 11).

The RMSE values of the misfit between the tide models and the spatiotemporally modeled PPP tidal estimates are less than 0.3 mm, and the TPXO8 tide model has lesser misfits. For the 25 SAR measurements, the spatiotemporally modeled OTL displacements of the PPP tidal estimates and the TPXO8 tide model are shown in Fig. 12.

The magnitude and spatial characteristics are mostly the same, and the most significant spatial OTL displacement reaches 14.1 mm. For a further explanation of the differences between the spatiotemporally modeled PPP tidal estimates and the results from the TPXO8 model, the RMSE misfit values of the spatial OTL displacements between the two methods at the pixels of the 25 SAR images were calculated (Fig. 13).

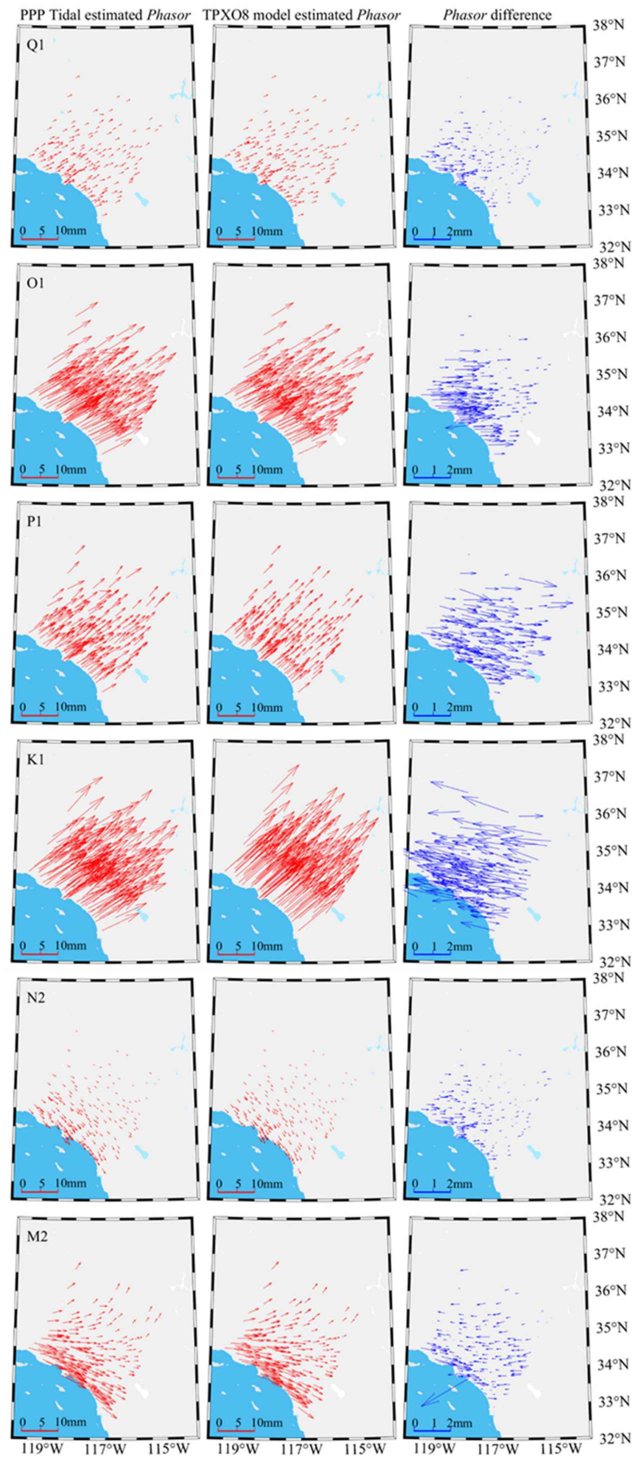

Fig. 9. *Phasor* estimated by the PPP tidal estimates and TPXO8 tide model, and the *phasor* difference between the two methods.

In Fig. 13, the RMSE values of pixels in inland areas are less than 0.4 mm, and a larger difference is seen between the spatiotemporally modeled PPP tidal displacement and the TPXO8 tide model displacement in areas close to the coastline. High-density GPS stations near the coastline can directly measure the OTL variations, and the temporally and spatially modeled PPP tidal estimates can reflect the OTL effect more accurately. Therefore, we used the spatiotemporally modeled

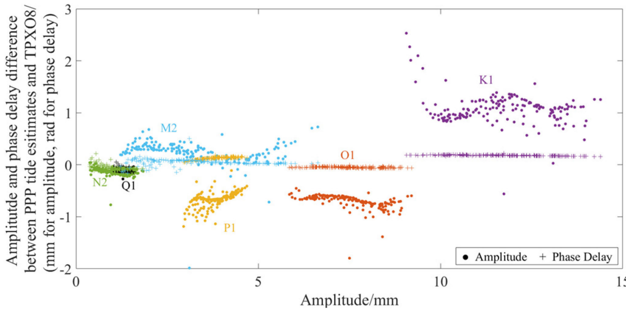

Fig. 10. Amplitude and phase delay difference between the PPP tide estimates and TPXO8 model.

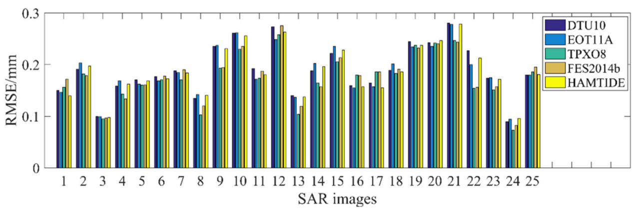

Fig. 11. RMSE values of the differences between the spatiotemporally modeled PPP tidal estimates and the OTL estimates of the tide models in the 25 SAR images.

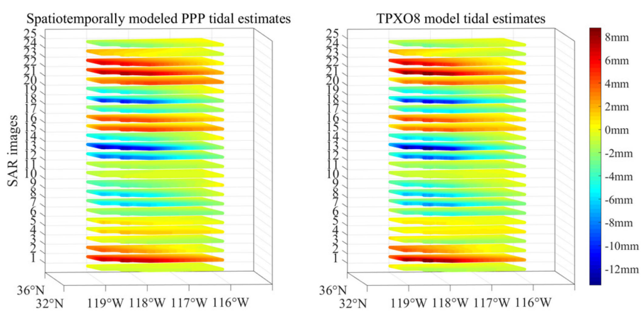

Fig. 12. Spatiotemporally modeled PPP tidal estimates and the TPXO8 model tidal estimates at the 25 SAR imaging times in the study area.

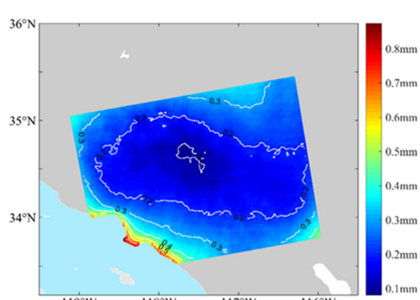

Fig. 13. RMSE misfit between the spatiotemporally modeled PPP estimates and the TPXO8 model tidal estimates at the pixels of the 25 SAR images.

PPP tidal displacements to correct the OTL in time-series InSAR measurements.

B. Correction of the OTL in InSAR Measurements

72 differential interferograms are generated from 25 Sentinel-1B SLC images according to the small baseline principle, and

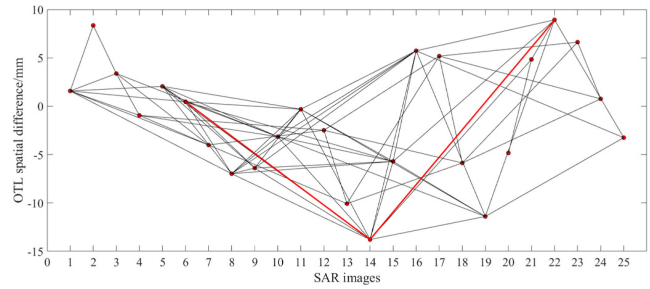

Fig. 14. Maximum spatial difference of the PPP tidal displacements in the 25 Sentinel-1B SAR images.

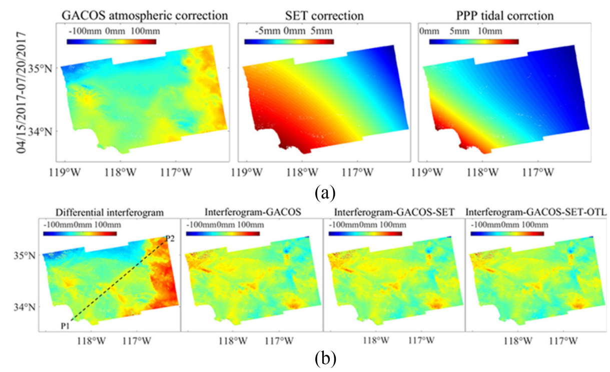

Fig. 15. (a) Correction of the atmospheric delay, SET, and spatiotemporally modeled PPP tidal displacements. (b) Corrections in the Sentinel-1B measurements acquired on April 15, 2017 and July 20, 2017.

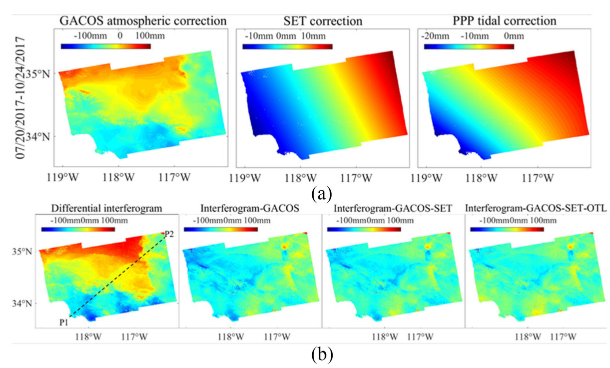

Fig. 16. (a) Correction of the atmospheric delay, SET, and spatiotemporally modeled PPP tidal displacements. (b) Corrections in the Sentinel-1B measurements acquired on July 20, 2017 and October 24, 2017.

the maximum spatial difference of OTL displacements in the 25 Sentinel-1B SAR images are calculated by using the PPP tidal displacements (Fig. 14).

We selected two differential interferograms as experimental samples (red line in Fig. 14), whose OTL effect is greater than 1.5 cm. The atmospheric delay in the interferogram is corrected by using the GACOS products, and the SET displacements are corrected using the SET correction model. In addition, the spatiotemporally modeled PPP tidal displacements are applied to correct the OTL in the interferogram (Figs. 15 and 16). The procedure of best planar fitting is not added in the data processing of the differential interferograms.

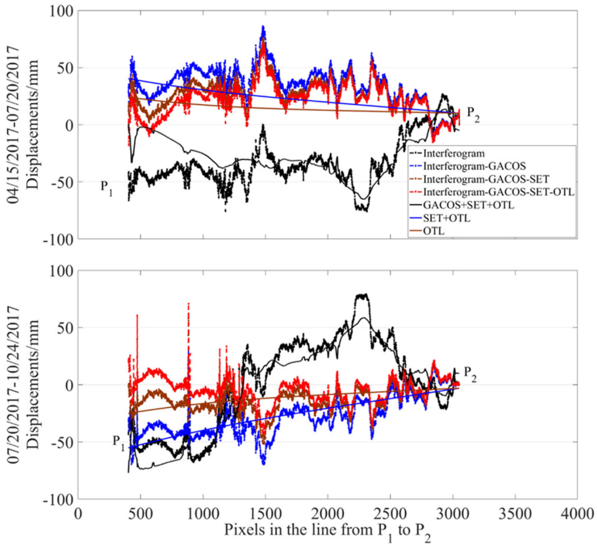

Fig. 17. Corrections of the GACOS, SET model, and spatiotemporally modeled PPP tide correction in the pixels of the line from P_1 to P_2.

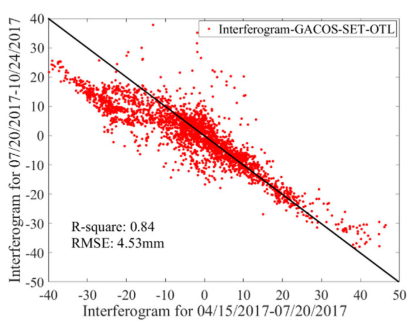

Fig. 18. Comparative analysis of the residual displacements in the line from P_1 to $P_2$of the differential interferograms of the 04/15/2017–07/20/2017 and 07/20/2017–10/24/2017 after the atmospheric delay, SET, and OTL corrected.

The atmospheric delay, SET, and OTL correction in the pixels of the line from P_1 to P_2 (Figs. 15 and 16) were conducted. The residuals in the Fig. 17 of the two selected interferograms after the corrections have high similarity. The orbital errors have been basically eliminated in the InSAR data processing. The large-scale signals in the unwrapped differential interferograms are mainly atmospheric delay errors, SET, and OTL signals. The topography-related errors in the interferograms are reduced after subtracting tropospheric corrections, and the small spatial-scale signals of the atmospheric turbulence, decorrelation noise, and crustal deformation still exist in the interferograms [35]. After the atmospheric delay is corrected, the trend signal in the interferograms is similar to the tidal displacements. Among the tidal displacements, the SET correction is close to the lower-order curve, and the spatiotemporally modeled PPP tidal estimates trend to the higher-order curve. The atmospheric delay, SET, and OTL corrected interferograms show that the spatial large-scale signals are substantially reduced.

The comparative analysis of the residual displacements after the atmospheric delay, SET, and OTL correction were conducted (Fig. 18). The residuals in the line from the point P_1 to point P_2 of the two selected interferograms showed a highly negative correlation, the R-square value is 0.84 and RMSE is 4.53 mm. In addition, the experimental results show that atmospheric delay error is the most important factor, but the tidal effect becomes a major signal in coastal areas that need to be corrected in the InSAR measurements. Particularly, the high-order OTL displacements in the coastal area cannot be removed by linear ramp.

V. Conclusion

In this article, we have proposed an approach for determining the spatiotemporal OTL effect in InSAR measurements. This approach uses the tidal harmonic function and the LSSVM method to estimate the spatiotemporal OTL displacements. An experiment based on Sentinel-1B measurements and regional GPS network data from the study area of Southern California was conducted, and the results showed that: 1) The spatial characteristics of the eight tidal constituents are very close to a high-order polynomial; 2) after the phasors of the tidal constituents are modeled by the polynomial kernel-based LSSVM method, the RMSE values of the difference between the spatiotemporally modeled PPP tidal estimates and the TPXO8 tide model estimates in the inland area are less than 0.4 mm. However, within a distance of 35 km from the coastline, it is found that there are larger misfits between the two methods. The spatiotemporally modeled PPP tidal estimates can provide higher precision spatial OTL displacements than TPXO8 model, in consideration of the lower accuracy and spatial resolution of the TPXO8 model in the offshore; and 3) the spatial large-scale signals in unwrapped differential interferogram of the Sentinel-1 measurements are mainly atmospheric delay, SET, and OTL effect, and the OTL signals can be corrected using the spatiotemporally modeled PPP tidal estimates. With this preparatory work, we have shown that the PPP tidal estimates can show the spatiotemporal variations of the OTL effect in InSAR measurements, and the correction of the high-order tides displacements is necessary for the InSAR data processing.

Acknowledgment

The GPS data were provided by SOPAC and processed in Bernese GPS software V5.2. The SPOTL program was used to produce the OTL correction. The Sentinel-1 dataset was provided by ESA (https://scihub.copernicus.eu/). The atmospheric delay maps were provided by GACOS (http://ceg-research.ncl.ac.uk/v2/gacos/). Part of the article was written while Wei Peng was visiting Texas State University.

References

[1] A. Hooper, D. Bekaert, K. Spaans, and M. Arikan, "Recent advances in SAR interferometry time series analysis for measuring crustal deformation," *Tectonophysics*, vol. 514–517, pp. 1–13, 2012.

[2] R. Jolivet *et al.*, "Improving InSAR geodesy using global atmospheric models," *J. Geophysical Res. Solid Earth*, vol. 119, no. 3, pp. 2324–2341, 2014.

[3] Y. Cao, Z. Li, J. Wei, J. Hu, M. Duan, and G. Feng, "Stochastic modeling for time series InSAR: With emphasis on atmospheric effects," *J. Geodesy*, vol. 92, no. 2, pp. 185–204, Feb. 2018.

[4] C. J. Dicaprio and M. Simons, "Importance of ocean tidal load corrections for differential InSAR," *Geophysical Res. Lett.*, vol. 35, no. 22, 2008, Art. no. L22309.

[5] W. Peng, Q. Wang, and Y. Cao, "Analysis of ocean tide loading in differential InSAR measurements," *Remote Sens.*, vol. 9, no. 2, 2017, Art. no 101.

[6] W. Peng, Q. Wang, and Y. Cao, "The extraction of ocean tidal loading from ASAR differential interferograms," *Sensors*, vol. 20, no. 3, Jan. 2020, Art. no. 632.
[7] A. Schubert, M. Jehle, D. Small, and E. Meier, "Mitigation of atmospheric perturbations and solid earth movements in a TerraSAR-X time-series," *J. Geodesy*, vol. 86, no. 4, pp. 257–270, Apr. 2012.
[8] C. Yu, Z. Li, N. T. Penna, and P. Crippa, "Generic atmospheric correction model for interferometric synthetic aperture radar observations," *J. Geophysical Res. Solid Earth*, vol. 123, no. 10, pp. 9202–9222, Oct. 2018.
[9] Q. Wang, W. Yu, B. Xu, and G. Wei, "Assessing the use of GACOS products for SBAS-INSAR deformation monitoring: A case in Southern California," *Sensors (Switzerland)*, vol. 19, no. 18, Sep. 2019, Art. no. 3894.
[10] K. Matsumoto, T. Takanezawa, and M. Ooe, "Ocean tide models developed by assimilating TOPEX/POSEIDON altimeter data into hydrodynamical model: A global model and a regional model around Japan," *J. Oceanogr.*, vol. 56, no. 5, pp. 567–581, 2000.
[11] F. Lyard, F. Lefevre, T. Letellier, and O. Francis, "Modelling the global ocean tides: Modern insights from FES2004," *Ocean Dyn.*, vol. 56, no. 5/6, pp. 394–415, Dec. 2006.
[12] G. D. Egbert and S. Y. Erofeeva, "Efficient inverse modeling of barotropic ocean tides," *J. Atmos. Ocean. Technol.*, vol. 19, no. 2, pp. 183–204, 2002.
[13] W. E. Farrell, "Deformation of the earth by surface loads," *Rev. Geophys.*, vol. 10, no. 3, pp. 761–797, 1972.
[14] C. C. Goad, "Gravimetric tidal loading computed from integrated Green's functions.," *J. Geophys. Res.*, vol. 85, no. B5, pp. 2679–2683, 1980.
[15] C. R. Allinson, P. J. Clarke, S. J. Edwards, M. A. King, T. F. Baker, and P. R. Cruddace, "Stability of direct GPS estimates of ocean tide loading," *Geophysical Res. Lett.*, vol. 31, no. 15, 2004, Art. No L020588.
[16] N. T. Penna, P. J. Clarke, M. S. Bos, and T. F. Baker, "Ocean tide loading displacements in western Europe: 1. Validation of kinematic GPS estimates," *J. Geophysical Res. Solid Earth*, vol. 120, no. 9, pp. 6523–6539, Sep. 2015.
[17] L. Yuan and B. F. Chao, "Analysis of tidal signals in surface displacement measured by a dense continuous GPS array," *Earth Planet. Sci. Lett.*, vol. 355–356, pp. 255–261, 2012.
[18] Y. Bock, L. Prawirodirdjo, and T. I. Melbourne, "Detection of arbitrarily large dynamic ground motions with a dense high-rate GPS network," *Geophysical Res. Lett.*, vol. 31, no. 6, Mar. 2004, Art. no. L019150.
[19] K. L. Feigl *et al.*, "Space geodetic measurement of crustal deformation in central and Southern California, 1984-1992," *J. Geophysical Res. Solid Earth*, vol. 98, no. B12, pp. 21677–21712, 1993.
[20] C. Urschl, R. Dach, U. Hugentobler, S. Schaer, and G. Beutler, "Validating ocean tide loading models using GPS," *J. Geodesy*, vol. 78, no. 10, pp. 616–625, 2005.
[21] N. T. Penna, M. A. King, and M. P. Stewart, "GPS height time series: Short-period origins of spurious long-period signals," *J. Geophysical Res. Solid Earth*, vol. 112, no. 2, Feb. 2007, Art. no. JB004047.
[22] L. G. Yuan, X. L. Ding, P. Zhong, W. Chen, and D. F. Huang, "Estimates of ocean tide loading displacements and its impact on position time series in Hong Kong using a dense continuous GPS network," *J. Geodesy*, vol. 83, no. 11, pp. 999–1015, 2009.
[23] J. A. K. Suykens and J. Vandewalle, "Least squares support vector machine classifiers," *Neural Process. Lett.*, vol. 9, no. 3, pp. 293–300, 1999.
[24] J. A. K. Suykens, T. Van Gestel, J. De Brabanter, B. De Moor, and J. Vandewalle, *Least Squares Support Vector Machines*. Singapore: World Scientific, 2002.
[25] U. Wegnüller, C. Werner, T. Strozzi, A. Wiesmann, O. Frey, and M. Santoro, "Sentinel-1 Support in the GAMMA Software," *Procedia Comput. Sci.*, vol. 100, pp. 1305–1312, 2016.
[26] P. Berardino, G. Fornaro, R. Lanari, and E. Sansosti, "A new algorithm for surface deformation monitoring based on small baseline differential SAR interferograms," *IEEE Trans. Geosci. Remote Sens.*, vol. 40, no. 11, pp. 2375–2383, Nov. 2002.
[27] K. E. Abraha, F. N. Teferle, A. Hunegnaw, and R. Dach, "GNSS related periodic signals in coordinate time-series from precise point positioning," *Geophysical J. Int.*, vol. 208, no. 3, pp. 1449–1464, 2017.
[28] Z. F. Yang, Z. W. Li, J. J. Zhu, J. Hu, Y. J. Wang, and G. L. Chen, "InSAR-based model parameter estimation of probability integral method and its application for predicting mining-induced horizontal and vertical displacements," *IEEE Trans. Geosci. Remote Sens.*, vol. 54, no. 8, pp. 4818–4832, Aug. 2016.
[29] G. Petit and B. Luzum, "IERS conventions (2010)," Federal Agency Cartography Geodesy BKG, Frankfurt, Germany, Tech. Rep. DTIC Document. 36, 2010.
[30] D. C. Agnew, "NLOADF: A program for computing ocean-tide loading," *J. Geophysical Res. Solid Earth*, vol. 102, no. B3, pp. 5109–5110, Mar. 1997.
[31] J. Marshall, M. Schenewerk, R. Snay, and S. Gutman, "The effect of the MAPS weather model on GPS-determined ellipsoidal heights," *GPS Solutions*, vol. 5, no. 1, pp. 1–14, Jul. 2001.
[32] M. King, "Kinematic and static GPS techniques for estimating tidal displacements with application to Antarctica," *J. Geodyn.*, vol. 41, no. 1/3, pp. 77–86, 2006.
[33] M. A. King, C. S. Watson, N. T. Penna, and P. J. Clarke, "Subdaily signals in GPS observations and their effect at semiannual and annual periods," *Geophysical Res. Lett.*, vol. 35, no. 3, 2008, Art. no. L032252.
[34] G. Wei, Q. Wang, and W. Peng, "Accurate evaluation of vertical tidal displacement determined by GPS kinematic precise point positioning: A case study of Hong Kong," *Sensors*, vol. 19, no. 11, Jun. 2019, Art. no. 2559.
[35] D. P. S. Bekaert, R. J. Walters, T. J. Wright, A. J. Hooper, and D. J. Parker, "Statistical comparison of InSAR tropospheric correction techniques," *Remote Sens. Environ.*, vol. 170, pp. 40–47, Dec. 2015.

Wei Peng received the master's degree in geodesy from Central South University, Changsha, China, in 2015, and the joint Ph.D. degree in geography from the Texas State University, San Marcos, Texas, USA, where he was sponsored by the China Scholarship Council (CSC), during Oct. 2017 to Oct. 2018. He is currently working toward the Ph.D. degree in geodesy with the Central South University, China.

His research interests include GPS and InSAR data processing, and environmental mass loading.

Qijie Wang received the Ph.D. degree in astrometry from Shanghai Astronomical Observatory, Chinese Academy of Sciences, in 2007.

She is a Professor with the School of Geosciences and Info-Physics, Central South University of China. Her main research interests includ InSAR deformation monitoring, remote sensing image processing, earth's rotation, and mechanism interpretation. Her current research focuses on tide correction for InSAR deformation monitoring and InSAR monitoring permafrost deformation. Her research has been supported by several projects of the National Natural Science Foundation of China.

F. Benjamin Zhan received the Ph.D. degree in geography from the State University of New York at Buffalo, NY, USA, in 1994.

He is the Professor of Geographic Information Science at Texas State University, San Marcos, TX, USA. He was the Founding Director of the Texas Center for Geographic Information Science at Texas State University and served as the First Director of the center from 2003 to 2015. He has authored or coauthored more than 120 peer-reviewed publications. His main research interests include health/medical geography, geographic information science, and spatial data science. His current research focuses on health disparities, cancer prevention, and environmental health. His research has been supported by various state and federal agencies in the USA.

Yunmeng Cao received the Ph.D. degree in geodesy from Central South University, Changsha, China, in 2019, and received the, joint Ph.D. degree in geophysics from the University of Miami, Coral Gables, FL, USA, where he was sponsored by the China Scholarship Council (CSC), during Oct. 2016 to Oct. 2018.

He is currently a Postdoctoral Fellow with King Abdullah University of Science and Technology (KAUST), Jeddah, Saudi Arabia, with the Crustal Deformation and InSAR Group (CDI), and working on satellite microwave remote sensing, particularly on InSAR-geodesy and geophysics.